

The “seesaw” impacts between reduced emissions and enhanced AOC on O₃ during the COVID-19

Shengqiang Zhu¹, James Poetzsch^{1,2}, Juanyong Shen³, Siyu Wang¹, Peng Wang^{4*}, Hongliang Zhang^{1,5*}

¹Department of Environmental Science and Engineering, Fudan University, Shanghai 200438, China

² School of Environmental Science and Engineering, Nanjing University of Information Science and Technology, 219 Ningliu Road, Nanjing 210044, China

³School of Environmental Science and Engineering, Shanghai Jiao Tong University, Shanghai 200240, China

⁴Department of Civil and Environmental Engineering, Hong Kong Polytechnic University, Hong Kong 99907, China

⁵Institute of Eco-Chongming (IEC), Shanghai 200062, China

*Corresponding authors: Peng Wang, peng.ce.wang@polyu.edu.hk; Hongliang Zhang, zhanghl@fudan.edu.cn.

Abstract

Due to the lockdown measures during the 2019 novel coronavirus (COVID-19) pandemic, the economic activities and the associated emissions have significantly declined. This reduction in emissions has created a natural experiment to assess the impact of the emitted precursor control policy on ozone (O₃) pollution, which has become a public concern in China during the last decade. In this study, we utilized comprehensive satellite, ground-level observations, and source-oriented chemical transport modeling to investigate the O₃ variations during the COVID-19 in China. Here we found that the O₃ formation regime shifted from a VOC-limited regime to a NO_x-limited regime due to the lower NO_x during the COVID-19 lockdown. However, instead of these changes of the O₃ formation region, the significant elevated O₃ in the North China Plain (40%) and Yangtze River Delta (35%) were mainly attributed to the enhanced atmospheric oxidant capacity (AOC) in these regions, which was different from previous studies. We suggest that future O₃ control policies should comprehensively consider the synergistic effects of O₃ formation regime and AOC on the O₃ elevation.

Introduction

Beginning in January 2020, a novel coronavirus (COVID-19) began rapidly spreading throughout China, first in Wuhan, and then in other major cities^{1,2}. In response, to prevent the spread of COVID-19, the first lockdown was implemented on January 23rd, suspending non-essential traffic in Wuhan, the epicenter of the outbreak. Over the following days, major cities throughout China issued similar travel restrictions and stringent lockdown measures, affecting over half a billion residents. These restrictive measures resulted in substantial reductions in human

activities, which consequently induced unprecedented decreases in anthropogenic emissions of air pollutants, especially from the industry and transportation sectors^{3, 4}. In particular, during the lockdown, NO₂ levels in Eastern China were estimated to have decreased by ~65% compared to the same period in 2019, mainly due to the reduction of vehicle emissions^{5, 6}. Similarly, other pollutants such as SO₂ and CO also decreased. In contrast, during the same period, ozone (O₃) increased significantly with a nationwide increase of 47.3%^{5, 7, 8}.

Besides the lockdown period, China experienced persistent O₃ pollutions in recent five years, especially in urban areas⁹⁻¹¹. O₃ is formed through non-linear photochemical reactions of nitrogen oxides (NO_x = NO + NO₂) and volatile organic compounds (VOCs)¹². The O₃ sensitivity regime, determined by the relative abundance of VOCs and NO_x, plays a significant role in O₃ formation^{13, 14}. Previous studies have reported that the elevated O₃ during lockdowns was mainly attributed to the enhanced atmospheric oxidation capacity (AOC)^{15, 16}, reflected by the levels of major oxidants such as hydroxyl radical (OH) and nitrate radical (NO₃)¹⁷. Specifically, NO₂ is defined as the main sink of OH radical through the reaction to form nitric acid (HNO₃)^{18, 19}. During the lockdown, the drastic decreases in NO₂ levels increased OH concentration, which then reacted with VOCs, facilitating the formation of secondary pollutants²⁰. Unfortunately, the current understanding of AOC and secondary pollution is still limited²¹⁻²³. The COVID-19 lockdown provides an important opportunity to study the interaction between emissions, AOC, and meteorological conditions.

In this study, we used observational and satellite data to identify changes in O₃ levels and its associated precursors (NO₂ and HCHO) during the COVID-19 lockdowns in China. The Community Multiscale Air Quality (CMAQ) model was also applied to analyze the characteristics of air quality in the same period. The roles of the O₃ sensitivity regime and AOC were also discussed to provide an in-depth explanation for the increase in O₃. We found that O₃ elevations during the COVID-19 lockdown period in the NCP and YRD were mainly controlled by enhanced AOC, even suppressing the impacts of the O₃ formation regime due to the reductions of anthropogenic emissions. In contrast, O₃ decreased slightly in the PRD. The results aim to formulate more effective emission control policies, particularly focused on reducing AOC to battle the persistent O₃ pollution in China.

Results

Significant O₃ variations during the Lockdown. Here we investigate O₃ changes during three periods around the COVID-19 Lockdown, which are defined as Pre-lockdown (January 6 to January 22, 2020), Lockdown (January 23 to February 29, 2020), and Post-lockdown (March 1 to March 31, 2020), respectively.

According to surface observation, changes in China's surface MDA8 O₃ show significant spatial variations from Pre-lockdown to Post-lockdown. During the Lockdown, elevated O₃ occurred in large areas throughout northern and central China, while it decreased in South China (Fig. 1a), consistent with previous studies^{5, 15, 24}. The most prominent O₃ increase occurred in the

NCP (Fig. 1b), with a mean MDA8 O₃ increase of 54% (from 24 ppb to 37 ppb) (Fig. 1c). In Baoding and Shijiazhuang (major cities in the NCP), O₃ increased by over 100%. Moreover, in the YRD, a noticeable MDA8 O₃ increase of 44% (from 26 ppb to 38 ppb) was observed. During Post-lockdown, observed O₃ concentrations continued to increase in the NCP and YRD, partially due to the rising temperature (Fig. S2). O₃ variation is more complex in the PRD, however. In general, O₃ levels decrease from Pre-lockdown to Post-lockdown. But in Guangzhou, the most populated city of PRD, an increase in O₃ was observed. Considering the similar temperature levels between Pre-lockdown and Lockdown over China, these variations are more related to the sudden reductions of O₃ precursors.

In addition, heightened O₃ pollution was observed in the NCP and YRD during the Lockdown compared to the same period in 2019 (Fig. S3). Although O₃ precursors decreased drastically in these regions, mean MDA8 O₃ levels were 14-19% higher than in 2019. In contrast, in the PRD, the mean MDA8 O₃ during the Lockdown of 2019 is close to (or even slightly higher) that in 2020, and the opposite of the trend observed in the other regions. Similar temperature conditions are also found during the Lockdown in 2019 and 2020, which fails to fully elucidate the O₃ differences between these two years, demonstrating that the emission reduction of O₃ precursors plays a more critical role in O₃ variations. Considering the O₃ results in the Lockdown periods in 2019 and 2020, it is critical to deeply understand the seesaw phenomenon between elevated O₃ and its reduced precursors.

Changes of O₃ precursors and formation regimes. Given that the ratio of HCHO to NO₂ determines the O₃ formation regimes, HCHO and NO₂ are considered the most important precursors of O₃²⁵. The satellite column data and CMAQ model have revealed significant reductions of NO₂ throughout much of China, especially in NCP and YRD regions (Fig S4a). According to the satellite data, NO₂ in the NCP, YRD, and PRD regions declined by 59.61%, 63.28%, and 44.03% during the Lockdown respectively. These reductions are mainly attributed to the significant decline of NO_x emissions from industry, power, and transportation sectors illustrated by the source apportionment analysis (Table. S6).

However, no noticeable changes were observed in the HCHO concentration during the Lockdown. The spatial distribution of HCHO, similar to that of NO₂, exhibits higher levels in southeast China, whereas in western China, due to the low anthropogenic VOCs emissions, the HCHO concentration is relatively low^{26,27}. The HCHO in the atmosphere is mainly formed through direct emissions from industrial and biogenic sectors and through secondary sources such as the oxidation reaction between VOCs and OH. During the Lockdown, emissions of HCHO and other VOCs declined significantly (-37%) in China (Table.S1) and therefore might have reduced HCHO levels. However, the enhanced AOC⁵ during Lockdown likely promoted the formation of HCHO from secondary sources, offsetting the impact of the decline in HCHO emissions and explaining why HCHO levels remained relatively constant. Also, the oxidation of methane, which has a long

lifetime and relatively stable concentrations, plays an important role in the HCHO concentration^{28, 29}, which also might help maintain constant HCHO levels as shown in our source apportionment analysis (Table.S6) during the Lockdown period.

In general, the O₃ sensitivity regimes in China shifted from VOC-limited to NO_x-limited during the Lockdown, as indicated by both satellite data and model simulations (Fig. 2b). During the Pre-Lockdown period in 2020, the VOC-limited regime dominates in the NCP, YRD, and PRD regions due to the relative abundant NO_x emissions from industry and transportation sectors, consistent with the previous studies³⁰. However, during the Lockdown period, VOC-limited regimes transitioned to NO_x-limited regimes in these regions. The percentage of NO_x-limited regimes in the NCP, YRD, and PRD regions during the Lockdown period increased from 11%, 37%, and 31% to 56%, 65%, and 69%, respectively. These changes in the O₃ formation regime and NO₂ and HCHO concentrations were not observed in 2019 (Fig. S5a); NO₂ and HCHO concentrations during the periods in 2019 that correspond to the Pre-lockdown and Lockdown periods in 2020 remained relatively constant, explaining the lack of variation in the O₃ formation regimes (Fig. S5b).

Surprisingly, O₃ levels increased in the NO_x-limited regimes in the NCP and YRD regions during the Lockdown period in 2020, even though pronounced reductions of NO_x levels were observed in these regions. This unusual phenomenon is contrary to previous studies²⁸, indicating that the enhanced AOC might have played a more significant role in increasing O₃ in these regions during the Lockdown period in 2020.

The dominating role of the enhanced AOC in O₃ formation. Our model simulations demonstrated significantly enhanced AOC in the NCP and YRD regions, which is consistent with the variation of O₃ concentrations. HO_x (OH and HO₂) radicals, the main daytime oxidant, increased significantly in central and northern China with the highest growth rates of 0.06 and 2.71 ppt for OH and HO₂ radical, respectively due to the relatively low levels of NO₂, the primary HO_x sink (Fig. 3a and Fig. S5a). Specifically, in the NCP, YRD, and PRD regions, the average increase in HO_x was 0.79, 0.92, and 0.17 ppt, respectively. The rise in OH and HO₂ radicals could be the leading cause of the O₃ increase during the Lockdown period in the NCP and YRD regions given their strong association with O₃ production³¹⁻³³.

The OH radicals oxidize VOCs to produce peroxy radicals such as HO₂, which convert NO to NO₂ without consuming O₃. Then the NO₂ produces O₃ through photolysis reactions, leading the O₃ accumulation^{34, 35}.

At the same time, the NO₃ radical, the primary nighttime oxidant, saw significantly increased levels in the NCP and YRD regions during the Lockdown, with respective growth rates of 0.49 and 0.29 ppt due to the relatively low levels of VOC and NO₂, both of which serve as important sinks for the NO₃ radical³⁶ (Fig. S6a). In contrast, in the PRD region, levels of the NO₃ radical declined (up to -0.21 ppt) (Fig. 3b-d). Given the enhanced AOC, a significant increase in O₃ was observed in the NCP and YRD regions. In the PRD, however, the constant AOC was responsible for a slight

decrease in O₃. Importantly, in the NCP and YRD regions, the increase in O₃ enhanced the AOC due to local photochemistry^{37, 38}, creating a vicious cycle of heightening O₃ levels.

O₃ control policy implications. Based on this analysis, we have devised a conceptual scheme to demonstrate the roles of the O₃ formation regime shift and enhanced AOC on O₃ level during the COVID-19 Lockdown period in China (Fig. 4). Satellite data and model simulations have revealed a pronounced shift in the O₃ formation regime during the 2020 lockdown period from VOC-limited to NO_x-limited, due to the significant decline in NO₂. Simultaneously, throughout much of China, the AOC was enhanced, facilitating the secondary formation of O₃ and HCHO in the atmosphere. Given the synergistic effects of enhanced AOC and the O₃ formation regime shift, a substantial increase in O₃ has occurred during the 2020 Lockdown period in much of China, particularly in the NCP and YRD regions. In contrast, O₃ levels during this period remained relatively stable in the PRD region. Our results have emphasized the importance of balanced emission control policies for reducing the O₃ pollution events in China. Previous policies, which have focused on the arbitrary reduction of primary emission of NO_x, SO₂, and VOCs, need to be reconsidered as different regions have different O₃ sensitivity, and current policies might unintentionally enhance AOC in certain regions, thereby heightening ozone levels. With the synergistic effects of O₃ formation regime and AOC, O₃ might be elevated in turn. In the future, we recommend that O₃ control policies of emission reduction utilize knowledge regarding the synergistic effect of O₃ formation regime and AOC variations in the atmosphere on O₃ levels. Specifically, we believe emission control policies ought to ensure a balance between emitted NO_x and VOCs to maintain stable O₃ formation regimes and thereby control O₃ emissions.

Reference

1. Hsiang, S. L.; Allen, D.; Annan-Phan, S.; Bell, K.; Bolliger, I.; Chong, T.; Druckenmiller, H.; Huang, L. Y.; Hultgren, A.; Krasovich, E.; Lau, P.; Lee, J.; Rolf, E.; Tseng, J.; Wu, T., The effect of large-scale anti-contagion policies on the COVID-19 pandemic (vol 93, pg 861, 2020). *Nature*.
2. Tisdell, C. A., Economic, social and political issues raised by the COVID-19 pandemic. *Economic analysis and policy* **2020**, *68*, 17-28.
3. Dai, Q.; Liu, B.; Bi, X.; Wu, J.; Liang, D.; Zhang, Y.; Feng, Y.; Hopke, P. K., Dispersion Normalized PMF Provides Insights into the Significant Changes in Source Contributions to PM_{2.5} after the COVID-19 Outbreak. *Environmental science & technology* **2020**, *54*, (16), 9917-9927.
4. Venter, Z. S.; Aunan, K.; Chowdhury, S.; Lelieveld, J., COVID-19 lockdowns cause global air pollution declines. *Proceedings of the National Academy of Sciences of the United States of America* **2020**, *117*, (32), 18984-18990.
5. Huang, X.; Ding, A.; Gao, J.; Zheng, B.; Zhou, D.; Qi, X.; Tang, R.; Wang, J.; Ren, C.; Nie, W., Enhanced secondary pollution offset reduction of primary emissions during COVID-19 lockdown in China. *National Science Review* **2020**.
6. Griffith, S. M.; Huang, W.-S.; Lin, C.-C.; Chen, Y.-C.; Chang, K.-E.; Lin, T.-H.; Wang, S.-H.; Lin, N.-H., Long-range air pollution transport in East Asia during the first week of the COVID-19 lockdown in China. *The Science of the total environment* **2020**, *741*, 140214.
7. Le, T.; Wang, Y.; Liu, L.; Yang, J.; Yung, Y. L.; Li, G.; Seinfeld, J. H., Unexpected air pollution with marked emission reductions during the COVID-19 outbreak in China. *Science* **2020**, eabb7431.
8. Zhao, Y.; Zhang, K.; Xu, X.; Shen, H.; Zhu, X.; Zhang, Y.; Hu, Y.; Shen, G., Substantial Changes in Nitrogen Dioxide and Ozone after Excluding Meteorological Impacts during the COVID-19 Outbreak in Mainland China. *Environmental Science & Technology Letters* **2020**, *7*, (6), 402-408.
9. Fang, X.; Park, S.; Saito, T.; Tunnicliffe, R.; Ganesan, A. L.; Rigby, M.; Li, S.; Yokouchi, Y.; Fraser, P. J.; Harth, C. M., Rapid increase in ozone-depleting chloroform emissions from China. *Nature Geoscience* **2019**, *12*, (2), 89-93.
10. Lu, X.; Hong, J.; Zhang, L.; Cooper, O. R.; Schultz, M. G.; Xu, X.; Wang, T.; Gao, M.; Zhao, Y.; Zhang, Y., Severe Surface Ozone Pollution in China: A Global Perspective. *Environmental Science & Technology Letters* **2018**, *5*, (8), 487-494.
11. Li, K.; Jacob, D. J.; Liao, H.; Shen, L.; Zhang, Q.; Bates, K. H., Anthropogenic drivers of 2013–2017 trends in summer surface ozone in China. *Proceedings of the National Academy of Sciences of the United States of America* **2019**, *116*, (2), 422-427.
12. Liu, Z.; Wang, Y.; Gu, D.; Zhao, C.; Huey, L. G.; Stickel, R.; Liao, J.; Shao, M.; Zhu, T.; Zeng, L.; Amoroso, A.; Costabile, F.; Chang, C.-C.; Liu, S.-C., Summertime photochemistry during CAREBeijing-2007: RO_x budgets and O₃ formation. *Atmospheric Chemistry and Physics (ACP) & Discussions (ACPD)* **2012**.

13. Jin, L.; Tonse, S.; Cohan, D. S.; Mao, X. L.; Harley, R. A.; Brown, N. J., Sensitivity analysis of ozone formation and transport for a central california air pollution episode. *Environmental Science & Technology* **2008**, *42*, (10), 3683-3689.
14. Lu, K. D.; Zhang, Y. H.; Su, H.; Brauers, T.; Chou, C. C.; Hofzumahaus, A.; Liu, S. C.; Kita, K.; Kondo, Y.; Shao, M.; Wahner, A.; Wang, J. L.; Wang, X. S.; Zhu, T., Oxidant (O₃ + NO₂) production processes and formation regimes in Beijing. *J. Geophys. Res.-Atmos.* **2010**, *115*.
15. Le, T.; Wang, Y.; Liu, L.; Yang, J.; Yung, Y. L.; Li, G.; Seinfeld, J. H., Unexpected air pollution with marked emission reductions during the COVID-19 outbreak in China. *Science (New York, N.Y.)* **2020**.
16. Goldstein, A. H.; Galbally, I. E., Known and unexplored organic constituents in the earth's atmosphere. *Environmental Science & Technology* **2007**, *41*, (5), 1514-1521.
17. Mochida, M.; Matsunaga, S.; Kawamura, K., A model evaluation of the NO titration technique to remove atmospheric oxidants for the determination of atmospheric organic compounds. *Environmental Science & Technology* **2003**, *37*, (8), 1589-1597.
18. Sadanaga, Y.; Yoshino, A.; Kato, S.; Kajii, Y., Measurements of OH reactivity and photochemical ozone production in the urban atmosphere. *Environmental Science & Technology* **2005**, *39*, (22), 8847-8852.
19. Chang, Y. H.; Zhang, Y. L.; Tian, C. G.; Zhang, S. C.; Ma, X. Y.; Cao, F.; Liu, X. Y.; Zhang, W. Q.; Kuhn, T.; Lehmann, M. F., Nitrogen isotope fractionation during gas-to-particle conversion of NO_x to NO₃⁻ in the atmosphere - implications for isotope-based NO_x source apportionment. *Atmos. Chem. Phys.* **2018**, *18*, (16), 11647-11661.
20. Yang, Y.; Wang, Y. H.; Zhou, P. T.; Yao, D.; Ji, D. S.; Sun, J.; Wang, Y. H.; Zhao, S. M.; Huang, W.; Yang, S. H.; Chen, D.; Gao, W. K.; Liu, Z. R.; Hu, B.; Zhang, R. J.; Zeng, L. M.; Ge, M. F.; Petaja, T.; Kerminen, V. M.; Kulmala, M.; Wang, Y. S., Atmospheric reactivity and oxidation capacity during summer at a suburban site between Beijing and Tianjin. *Atmos. Chem. Phys.* **2020**, *20*, (13), 8181-8200.
21. Shiu, C. J.; Liu, S. C.; Chang, C. C.; Chen, J. P.; Chou, C. C. K.; Lin, C. Y.; Young, C. Y., Photochemical production of ozone and control strategy for Southern Taiwan. *Atmos. Environ.* **2007**, *41*, (40), 9324-9340.
22. Feng, T.; Zhao, S. Y.; Bei, N. F.; Wu, J. R.; Liu, S. X.; Li, X.; Liu, L.; Qian, Y.; Yang, Q. C.; Wang, Y. C.; Zhou, W. J.; Cao, J. J.; Li, G. H., Secondary organic aerosol enhanced by increasing atmospheric oxidizing capacity in Beijing-Tianjin-Hebei (BTH), China. *Atmos. Chem. Phys.* **2019**, *19*, (11), 7429-7443.
23. Sheehy, P. M.; Volkamer, R.; Molina, L. T.; Molina, M. J., Oxidative capacity of the Mexico City atmosphere - Part 2: A RO_x radical cycling perspective. *Atmos. Chem. Phys.* **2010**, *10*, (14), 6993-7008.
24. Zhao, Y. B.; Zhang, K.; Xu, X. T.; Shen, H. Z.; Zhu, X.; Zhang, Y. X.; Hu, Y. T.; Shen, G. F., Substantial Changes in Nitrogen Dioxide and Ozone after Excluding Meteorological Impacts

during the COVID-19 Outbreak in Mainland China. *Environ. Sci. Technol. Lett.* **2020**, *7*, (6), 402-408.

25. Jin, X. M.; Fiore, A. M.; Murray, L. T.; Valin, L. C.; Lamsal, L. N.; Duncan, B.; Folkert Boersma, K.; De Smedt, I.; Abad, G. G.; Chance, K.; Tonnesen, G. S., Evaluating a Space-Based Indicator of Surface Ozone-NO_x-VOC Sensitivity Over Midlatitude Source Regions and Application to Decadal Trends. *J. Geophys. Res.-Atmos.* **2017**, *122*, (19), 10231-10253.
26. Bo, Y.; Cai, H.; Xie, S. D., Spatial and temporal variation of historical anthropogenic NMVOCs emission inventories in China. *Atmos. Chem. Phys.* **2008**, *8*, (23), 7297-7316.
27. Li, M.; Zhang, Q.; Zheng, B.; Tong, D.; Lei, Y.; Liu, F.; Hong, C. P.; Kang, S. C.; Yan, L.; Zhang, Y. X.; Bo, Y.; Su, H.; Cheng, Y. F.; He, K. B., Persistent growth of anthropogenic non-methane volatile organic compound (NMVOC) emissions in China during 1990-2017: drivers, speciation and ozone formation potential. *Atmos. Chem. Phys.* **2019**, *19*, (13), 8897-8913.
28. Jin, X. M.; Holloway, T., Spatial and temporal variability of ozone sensitivity over China observed from the Ozone Monitoring Instrument. *J. Geophys. Res.-Atmos.* **2015**, *120*, (14), 7229-7246.
29. Boeke, N. L.; Marshall, J. D.; Alvarez, S.; Chance, K. V.; Fried, A.; Kurosu, T. P.; Rappengluck, B.; Richter, D.; Walega, J.; Weibring, P.; Millet, D. B., Formaldehyde columns from the Ozone Monitoring Instrument: Urban versus background levels and evaluation using aircraft data and a global model. *J. Geophys. Res.-Atmos.* **2011**, *116*, 11.
30. Xing, J.; Wang, S. X.; Jang, C.; Zhu, Y.; Hao, J. M., Nonlinear response of ozone to precursor emission changes in China: a modeling study using response surface methodology. *Atmospheric Chemistry and Physics* **2011**, *11*, (10), 5027-5044.
31. Ren, X. R.; van Duin, D.; Cazorla, M.; Chen, S.; Mao, J. Q.; Zhang, L.; Brune, W. H.; Flynn, J. H.; Grossberg, N.; Lefer, B. L.; Rappengluck, B.; Wong, K. W.; Tsai, C.; Stutz, J.; Dibb, J. E.; Jobson, B. T.; Luke, W. T.; Kelley, P., Atmospheric oxidation chemistry and ozone production: Results from SHARP 2009 in Houston, Texas. *J. Geophys. Res.-Atmos.* **2013**, *118*, (11), 5770-5780.
32. Kentarchos, A. S.; Roelofs, G. J., A model study of stratospheric ozone in the troposphere and its contribution to tropospheric OH formation. *J. Geophys. Res.-Atmos.* **2003**, *108*, (D12), 9.
33. Zhang, Q.; Yuan, B.; Shao, M.; Wang, X.; Lu, S.; Lu, K.; Wang, M.; Chen, L.; Chang, C. C.; Liu, S. C., Variations of ground-level O₃ and its precursors in Beijing in summertime between 2005 and 2011. *Atmos. Chem. Phys.* **2014**, *14*, (12), 6089-6101.
34. Pollack, I. B.; Ryerson, T. B.; Trainer, M.; Neuman, J. A.; Roberts, J. M.; Parrish, D. D., Trends in ozone, its precursors, and related secondary oxidation products in Los Angeles, California: A synthesis of measurements from 1960 to 2010. *J. Geophys. Res.-Atmos.* **2013**, *118*, (11), 5893-5911.
35. Tan, Z. F.; Lu, K. D.; Jiang, M. Q.; Su, R.; Wang, H. L.; Lou, S. R.; Fu, Q. Y.; Zhai, C. Z.; Tan, Q. W.; Yue, D. L.; Chen, D. H.; Wang, Z. S.; Xie, S. D.; Zeng, L. M.; Zhang, Y. H., Daytime

atmospheric oxidation capacity in four Chinese megacities during the photochemically polluted season: a case study based on box model simulation. *Atmospheric Chemistry and Physics* **2019**, *19*, (6), 3493-3513.

36. Lucas, D. D.; Prinn, R. G., Parametric sensitivity and uncertainty analysis of dimethylsulfide oxidation in the clear-sky remote marine boundary layer. *Atmos. Chem. Phys.* **2005**, *5*, 1505-1525.

37. Asaf, D.; Pedersen, D.; Matveev, V.; Peleg, M.; Kern, C.; Zingler, J.; Platt, U.; Luria, M., Long-Term Measurements of NO₃ Radical at a Semiarid Urban Site: 1. Extreme Concentration Events and Their Oxidation Capacity. *Environmental Science & Technology* **2009**, *43*, (24), 9117-9123.

38. Geyer, A.; Alicke, B.; Konrad, S.; Schmitz, T.; Stutz, J.; Platt, U., Chemistry and oxidation capacity of the nitrate radical in the continental boundary layer near Berlin. *J. Geophys. Res.-Atmos.* **2001**, *106*, (D8), 8013-8025.

Figures

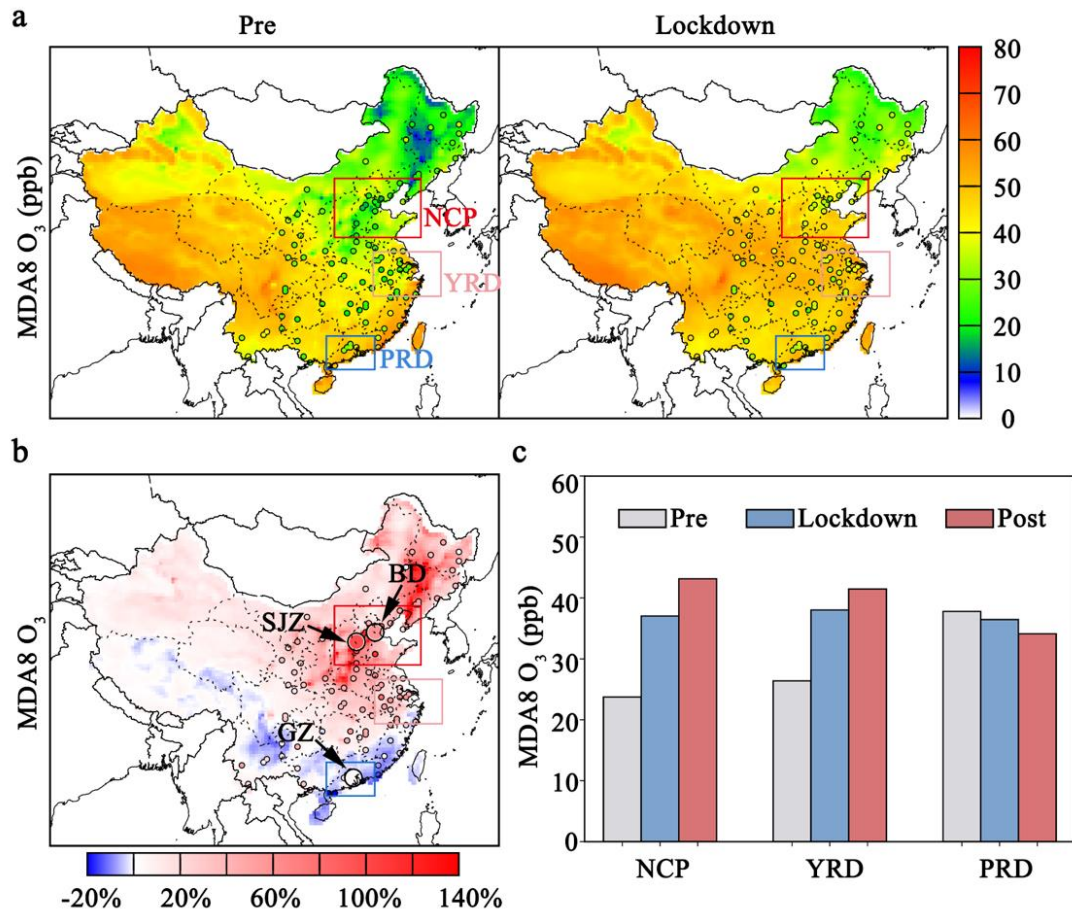


Fig. 1 MDA8 O₃ changes in China during the Pre-lockdown and Lockdowns. (a) CMAQ predicted and observed surface MDA8 O₃ in China during Pre-lockdown and Lockdown periods. The dots represent the observed MDA8 O₃ values; SJZ: Shijiazhuang; BD: Baoding; GZ: Guangzhou. (b) Observed and simulated MDA8 O₃ growth rate during Pre-lockdown and Lockdown periods. (c) Observed mean MDA8 O₃ in the NCP, YRD, and PRD regions.

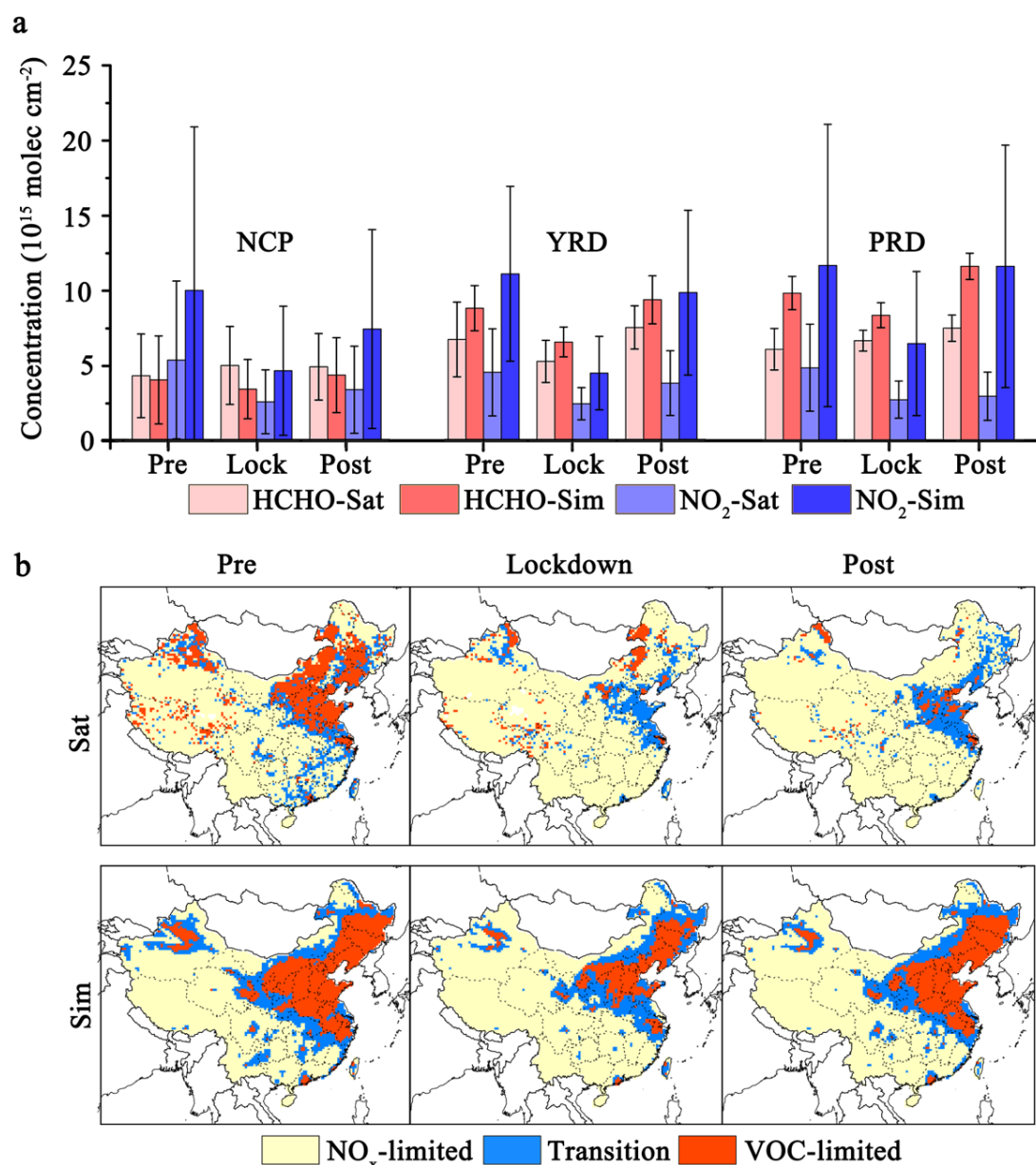


Fig. 2 The spatial distribution of NO₂ and HCHO and the O₃ formation regime in China. **(a)** The CMAQ predicted results and Tropomi satellite results for NO₂ and HCHO column concentrations in NCP, YRD, and PRD regions during the Pre-lockdown, Lockdown, and Post-lockdown periods. **(b)** The predicted and satellite observed results of the O₃ formation regime in the troposphere during the Pre-lockdown, Lockdown, and Post-lockdown periods in China.

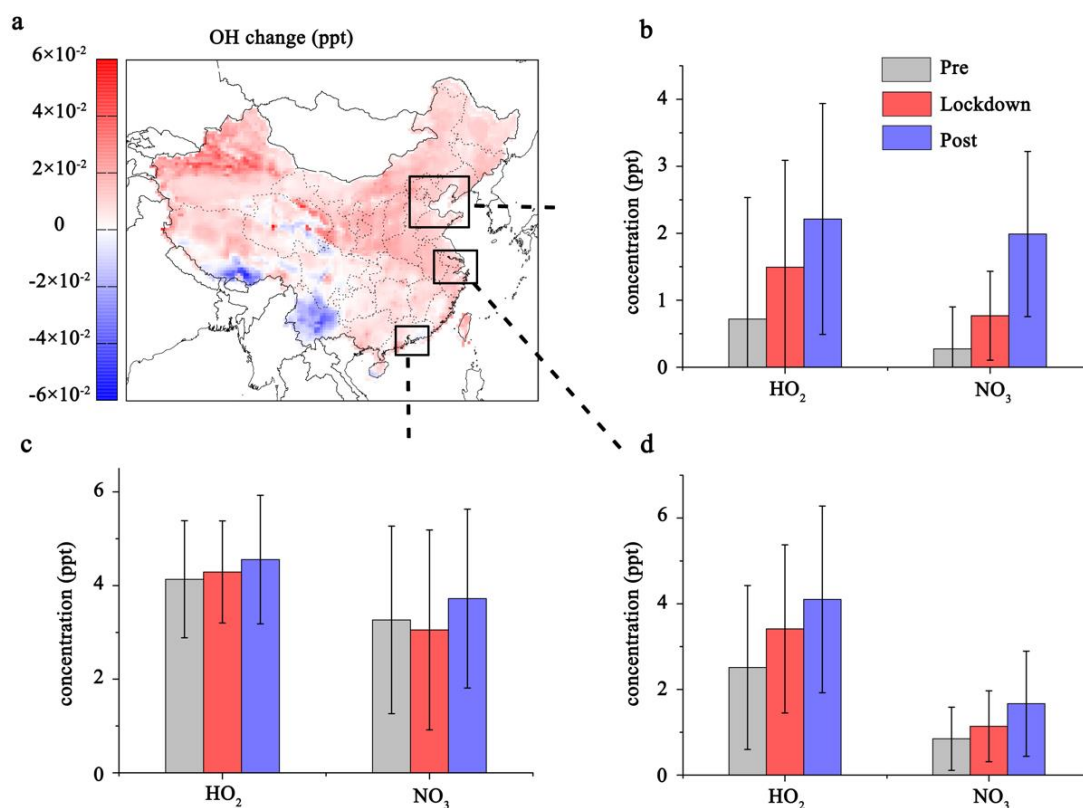


Fig. 3 Major oxidants changes during the Pre-lockdown and Lockdown. (a) The spatial distribution variation of simulated OH radical during the Lockdown and Pre-Lockdown periods. (b-d) The averaged ground-level concentrations of HO_2 and NO_3 radicals during the Pre-lockdown, Lockdown, and Post-lockdown periods in NCP, YRD, and PRD regions.

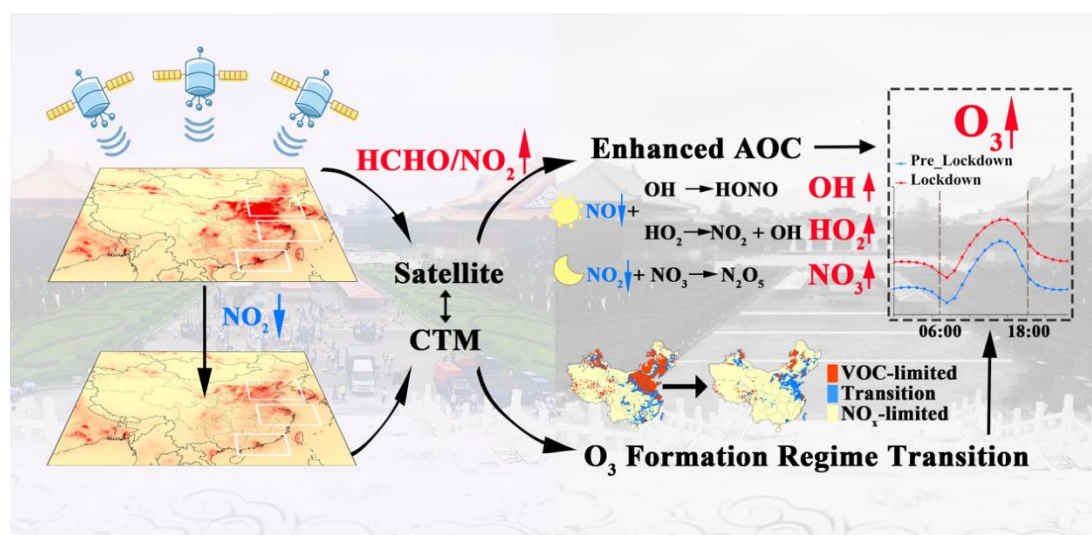


Fig. 4 Conceptual frame representing the synergistic effect of enhanced AOC and O_3 formation regime shift. The left panel illustrates the decline in NO_2 during the Lockdown. The right panel demonstrates the synergistic effect of enhanced AOC and the O_3 formation regime shift responsible for the increase in O_3 .

Supplementary Information for
The “seesaw” impacts between reduced emissions and enhanced
AOC on O₃ during the COVID-19

Shengqiang Zhu¹, James Poetzscher^{1,2}, Juanyong Shen³, Siyu Wang¹, Peng Wang⁴, Hongliang
Zhang^{1,5}

¹Department of Environmental Science and Engineering, Fudan University, Shanghai 200438,
China

²School of Environmental Science and Engineering, Nanjing University of Information Science
and Technology, 219 Ningliu Road, Nanjing 210044, China

³School of Environmental Science and Engineering, Shanghai Jiao Tong University, Shanghai
200240, China

⁴Department of Civil and Environmental Engineering, Hong Kong Polytechnic University, Hong
Kong 99907, China

⁵Institute of Eco-Chongming (IEC), Shanghai 200062, China

*Corresponding authors: Peng Wang, peng.ce.wang@polyu.edu.hk; Hongliang Zhang,
zhanghl@fudan.edu.cn.

This file includes Supplementary text, and Supplementary Figure S1-S6, Supplementary Table S1-S7

Supplementary text

Method

The Sentinel-5 Precursor (S-5P) is a satellite launched by the European Space Agency (ESA) in October 2017 to monitor the spatiotemporal variation of air pollutants, greenhouse gases, UV radiation, and clouds, worldwide. The onboard sensor, TROPOMI (TROPOspheric Monitoring Instrument), has a sun-synchronous orbit with a local overpass time of approximately 13:30 and near-daily global coverage¹⁻³. TROPOMI data products are significantly improved compared to the still operating OMI sensor, launched in 2004; specifically, TROPOMI data products feature significantly increased spatial resolution and 1~5 times higher signal-to-noise ratios, compared to OMI products⁴. On August 6, 2019, TROPOMI began outputting data at a higher resolution than before (each near-nadir pixel size is now roughly $5.5 \times 3.5 \text{ km}^2$)⁵.

TROPOMI products are available for free through the Copernicus Open Access Hub (<https://scihub.copernicus.eu>, last access: 30th July, 2020). Google Earth Engine (<https://developers.google.com/earth-engine/datasets/catalog>, last access: 30th July, 2020) has converted Level 2 TROPOMI data, provided by the Copernicus Open Access Hub, into the level 3 data used in this study through the bin_spatial operation for the harpconvert tool. In this study, we utilized two TROPOMI datasets from Google Earth Engine, tropospheric NO₂ column number density, and tropospheric HCHO column number density, and re-projected them into the same domain as model simulations by using a Lambert projection. As suggested by Copernicus, Google Earth Engine filters the source data to remove pixels with QA values less than 75% for tropospheric NO₂ column number density datasets and 50% for tropospheric HCHO column number density.

Model configuration and validation

A modified CMAQ model v5.0.2 with an expanded SAPRC-99 photochemical mechanism was applied to simulate the O₃ levels and track the sources of its precursors in China. The details of the source-tracking technique have been described in many previous studies⁶⁻⁹ and thus are not discussed here. The time interval for which the simulation was conducted spanned from January 1 to March 31, comprising the Pre-lockdown (January 6 to 22), Lockdown (January 23 to February 29), and Post-lockdown (March 1 to 31) periods. Simulations for the same period in 2019, a control period during which there were no emission reductions due to the COVID-19 induced lockdowns, were also conducted. The first five days (January 1-5 in 2019 and 2020) during the simulation periods were chosen as spin-up and removed from the subsequent analysis. The model domain included China and its surrounding countries (Fig. S1), with a horizontal resolution of $36 \text{ km} \times 36 \text{ km}$ (127×197 grids). The vertical extent was ~20 km from the surface and divided into 18 sigma layers with the first layer height at a height of ~35 m from the surface. The anthropogenic emissions comprised of agriculture, industry, power, residential, and transportation sectors were based on the Multi-resolution Emission Inventory for China (MEIC, v1.3, $0.25^\circ \times 0.25^\circ$, <http://www.meicmodel.org>). The anthropogenic emissions of different pollutants in China during

the Lockdown were adjusted according to a recent study to reflect the reduced human activity (Table S1)¹⁰. Emissions from other countries were obtained from the Emissions Database for Global Atmospheric Research (EDGAR) v4.3.1 (<https://edgar.jrc.ec.europa.eu/overview.php?v=431>). Biogenic emissions were provided by the Model of Emissions of Gases and aerosols from Nature (MEGAN) v2.1¹¹. The meteorological inputs were generated by the Weather Research and Forecasting (WRF) model v4.2 (<https://www2.mmm.ucar.edu/wrf/users>), with the initial and boundary conditions based on the National Centers for Environmental Prediction (NCEP) Final (FNL) Operational Model Global Tropospheric Analyses dataset (<https://rda.ucar.edu/datasets/ds083.2>).

The WRF model performance was evaluated by comparing the predicted temperature (T), relative humidity (RH) at 2 m above the surface, wind speed (WS), and wind direction (WD) at 10 m above the surface with observation data from the National Climatic Data Center (<ftp://ftp.ncdc.noaa.gov/pub/data/noaa/>) (~1400 sites) (Table S2, S4). The model slightly underestimated the T during the simulation periods, with the mean bias (MB) values of -1.35 to -0.43 similar to a previous study¹². The gross error (GE) values (1.65-1.93) of WS were all within the benchmark¹³. The WD was generally predicted successfully, with values around the benchmarks. The simulation of RH was comparable with previous studies^{12, 14, 15}. Overall, the WRF model performed well, providing the CMAQ model with reliable meteorological inputs.

The CMAQ model simulations were validated using the observations (~1500 sites) from the national air quality monitoring network (<http://www.cnemc.cn/>) (Table S3-S5). The model accurately predicted the hourly O₃ concentrations, with mean normalized bias (MNB) values of 0.04-0.13 and mean normalized error (MNE) values ranging from 0.09 to 0.17, which were all within the criteria^{16, 17}. The simulations of O₃-8h were slightly overestimated with MNB values of 0.18-0.21, a little higher than the criteria.

The changes in O₃, NO₂, and SO₂ during the simulation periods were accurately captured by the model. In general, the model performed well, accurately simulating O₃ levels throughout the analyzed time periods.

NO₂ and HCHO concentrations from 17 vertical layers (with the highest layer having a height of ~10km) in the CMAQ model were added up to ascertain their tropospheric column concentrations. The NO₂ and HCHO column concentrations generated by the model were then compared with the satellite data to determine the shift in O₃ formation regimes. In our study, the O₃ formation regimes were categorized into VOC-limited, NO_x-limited and transition regimes based on the formaldehyde nitrogen ratio (FNR)^{18, 19}. Here we set FNR < 1.0 as a VOC-limited regime, FNR > 2.0 as a NO_x-limited regime and FNR between 1.0 and 2.0 as a transitional regime^{20, 21}.

Supplement formula

The mean bias (MB), gross error (GE), and root mean square error (RMSE) were used for the evaluation of WRF model performance, while the mean normalized bias (MNB), mean normalized error (MNE), mean fractional bias (MFB) and mean fractional error (MFE) were used for the

validation of CMAQ model performance.

MB

$$= \frac{1}{N} \sum_{i=1}^N (C_{m,i} - C_{o,i}) \quad (1)$$

GE

$$= \frac{1}{N} \sum_{i=1}^N |C_{m,i} - C_{o,i}| \quad (2)$$

RMSE

$$= \left(\frac{1}{N} \sum_{i=1}^N (C_{m,i} - C_{o,i})^2 \right)^{\frac{1}{2}} \quad (3)$$

MNB

$$= \frac{1}{N} \sum_{i=1}^N \frac{C_{m,i} - C_{o,i}}{C_{o,i}} \quad (4)$$

MNE

$$= \frac{1}{N} \sum_{i=1}^N \frac{|C_{m,i} - C_{o,i}|}{C_{o,i}} \quad (5)$$

MFB

$$= \frac{2}{N} \sum_{i=1}^N \frac{C_{m,i} - C_{o,i}}{C_{m,i} + C_{o,i}} \quad (6)$$

MFE

$$= \frac{2}{N} \sum_{i=1}^N \frac{|C_{m,i} - C_{o,i}|}{C_{m,i} + C_{o,i}} \quad (7)$$

where $C_{m,i}$ and $C_{o,i}$ refer to the i^{th} predicted and observed value, respectively. N is the number of prediction-observation pairs drawn from all measurement sites.

Reference

1. Liu, F.; Page, A.; Strode, S. A.; Yoshida, Y.; Choi, S.; Zheng, B.; Lamsal, L. N.; Li, C.; Krotkov, N. A.; Eskes, H.; van der A, R.; Veefkind, P.; Levelt, P. F.; Hauser, O. P.; Joiner, J., Abrupt decline in tropospheric nitrogen dioxide over China after the outbreak of COVID-19. *Sci. Adv.* **2020**, *6*, (28), 5.
2. Ogen, Y., Assessing nitrogen dioxide (NO₂) levels as a contributing factor to coronavirus (COVID-19) fatality. *Science of the Total Environment* **2020**, 726, 5.
3. Veefkind, J. P.; Aben, I.; McMullan, K.; Förster, H.; de Vries, J.; Otter, G.; Claas, J.; Eskes, H. J.; de Haan, J. F.; Kleipool, Q.; van Weele, M.; Hasekamp, O.; Hoogeveen, R.; Landgraf, J.; Snel, R.; Tol, P.; Ingmann, P.; Voors, R.; Kruizinga, B.; Vink, R.; Visser, H.; Levelt, P. F., TROPOMI on the ESA Sentinel-5 Precursor: A GMES mission for global observations of the atmospheric composition for climate, air quality and ozone layer applications. *Remote Sensing of Environment* **2012**, *120*, 70-83.
4. Pei, Z.; Han, G.; Ma, X.; Su, H.; Gong, W., Response of major air pollutants to COVID-19 lockdowns in China. *Science of The Total Environment* **2020**, 743, 140879.
5. Huang, G.; Sun, K., Non-negligible impacts of clean air regulations on the reduction of tropospheric NO₂ over East China during the COVID-19 pandemic observed by OMI and TROPOMI. *Science of The Total Environment* **2020**, 745, 141023.
6. Wang, P.; Wang, T.; Ying, Q., Regional source apportionment of summertime ozone and its precursors in the megacities of Beijing and Shanghai using a source-oriented chemical transport model. *Atmospheric Environment* **2020**, 224, 117337.
7. Ying, Q.; Krishnan, A., Source contributions of volatile organic compounds to ozone formation in southeast Texas. *Journal of Geophysical Research: Atmospheres* **2010**, *115*, (D17).
8. Zhang, H.; Ying, Q., Contributions of local and regional sources of NO_x to ozone concentrations in Southeast Texas. *Atmospheric Environment* **2011**, *45*, (17), 2877-2887.
9. Wang, P.; Chen, Y.; Hu, J.; Zhang, H.; Ying, Q., Source apportionment of summertime ozone in China using a source-oriented chemical transport model. *Atmospheric Environment* **2019**, *211*, 79-90.
10. Huang, X.; Ding, A.; Gao, J.; Zheng, B.; Zhou, D.; Qi, X., ... He, K., Enhanced secondary pollution offset reduction of primary emissions during COVID-19 lockdown in China. *EarthArXiv* **2020**, April 13.
11. Guenther, A. B.; Jiang, X.; Heald, C. L.; Sakulyanontvittaya, T.; Duhl, T.; Emmons, L. K.; Wang, X., The Model of Emissions of Gases and Aerosols from Nature version 2.1 (MEGAN2.1): an extended and updated framework for modeling biogenic emissions. *Geoscientific Model Development (GMD)* **2012**, *5*, (6), 1471-1492.
12. Shen, J.; Zhao, Q.; Cheng, Z.; Wang, P.; Ying, Q.; Liu, J.; Duan, Y.; Fu, Q., Insights into source origins and formation mechanisms of nitrate during winter haze episodes in the Yangtze River Delta. *Science of The Total Environment* **2020**, 741, 140187.
13. Emery, C.; Tai, E.; Yarwood, G. In *Enhanced meteorological modeling and performance evaluation for two texas episodes*, In: Report to the Texas Natural Resources Conservation Commission. p.b.E., International Corp (Ed.), Novato, CA., 2001; 2001.
14. Hu, J.; Wang, P.; Ying, Q.; Zhang, H.; Chen, J.; Ge, X.; Li, X.; Jiang, J.; Wang, S.; Zhang, J., Modeling biogenic and anthropogenic secondary organic aerosol in China. *Atmospheric Chemistry and Physics* **2016**, *17*, (1), 77-92.

15. Zhang, H.; Li, J.; Ying, Q.; Yu, J. Z.; Wu, D.; Cheng, Y.; He, K.; Jiang, J., Source apportionment of PM_{2.5} nitrate and sulfate in China using a source-oriented chemical transport model. *Atmospheric Environment* **2012**, 62, (62), 228-242.
16. EPA, U., Guidance on the Use of Models and Other Analyses in Attainment Demonstrations for the 8-hour Ozone. *NAAQSRep* **2005**, EPA-454/R-05-002.
17. EPA, U., Guidance on the use of models and other analyses for demonstrating attainment of air quality goals for ozone, PM_{2.5}, and regional haze. *US Environmental Protection Agency* **2007**, Office of Air Quality Planning and Standards.
18. Tang, G.; Wang, Y.; Li, X.; Ji, D.; Hsu, S.; Gao, X., Spatial-temporal variations in surface ozone in Northern China as observed during 2009-2010 and possible implications for future air quality control strategies. *Atmos. Chem. Phys.* **2012**, 12, (5), 2757-2776.
19. Jin, X. M.; Holloway, T., Spatial and temporal variability of ozone sensitivity over China observed from the Ozone Monitoring Instrument. *J. Geophys. Res.-Atmos.* **2015**, 120, (14), 7229-7246.
20. Duncan, B. N.; Yoshida, Y.; Olson, J. R.; Sillman, S.; Martin, R. V.; Lamsal, L.; Hu, Y. T.; Pickering, K. E.; Retscher, C.; Allen, D. J.; Crawford, J. H., Application of OMI observations to a space-based indicator of NO_x and VOC controls on surface ozone formation. *Atmos. Environ.* **2010**, 44, (18), 2213-2223.
21. Witte, J. C.; Duncan, B. N.; Douglass, A. R.; Kurosu, T. P.; Chance, K.; Retscher, C., The unique OMI HCHO/NO₂ feature during the 2008 Beijing Olympics: Implications for ozone production sensitivity. *Atmos. Environ.* **2011**, 45, (18), 3103-3111.

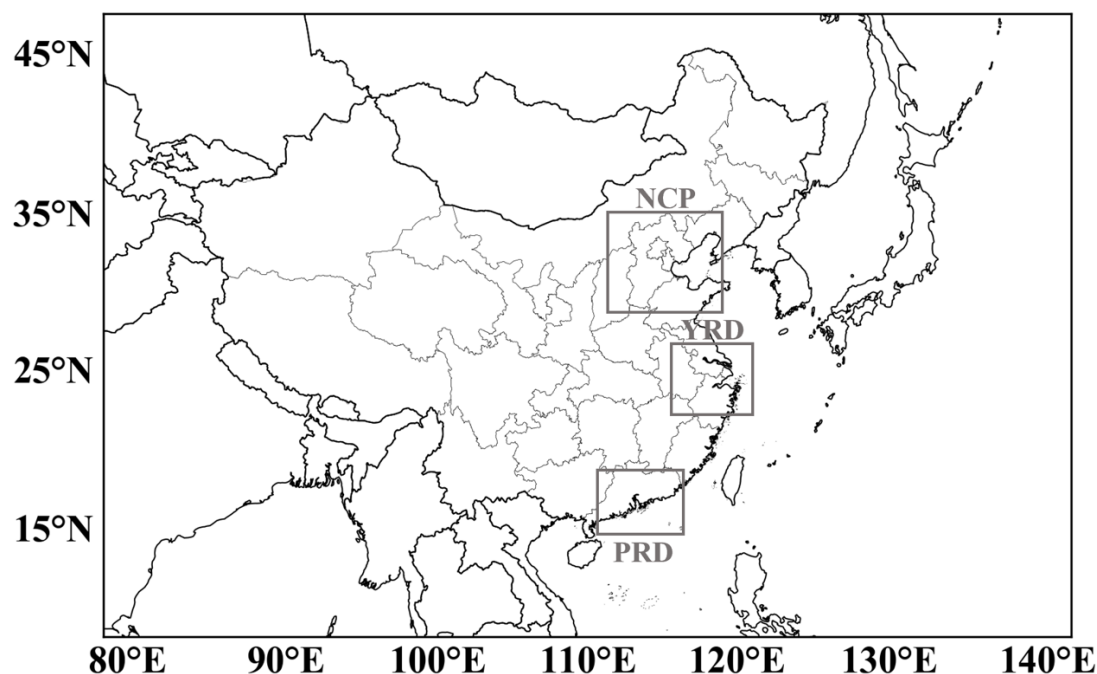


Figure S1: Model domain and three subregions (NCP, YRD, and PRD).

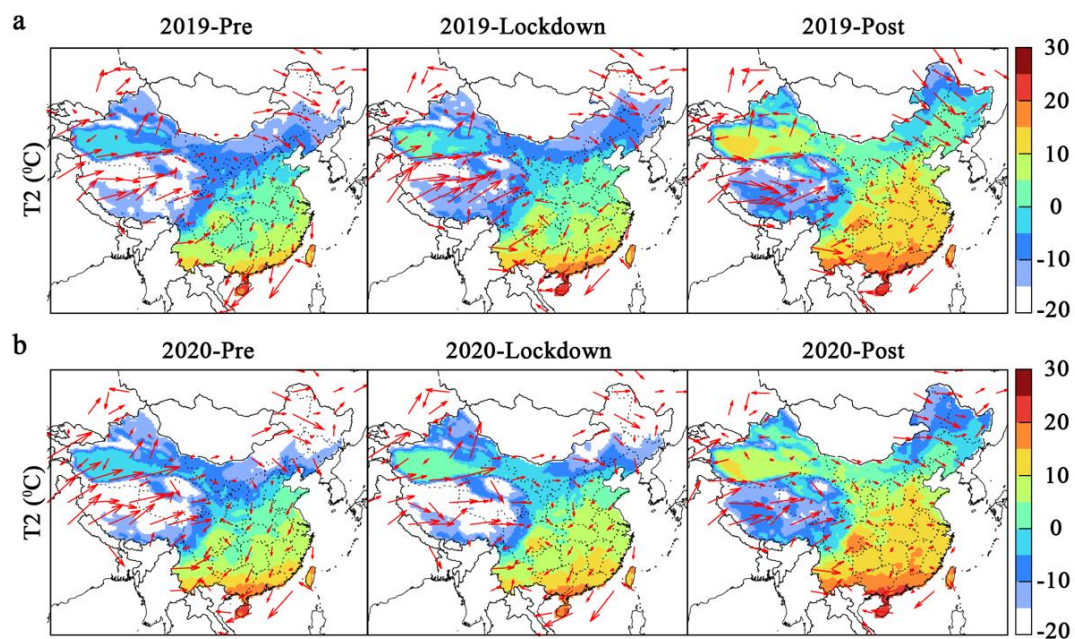


Figure S2: Regional variation of the temperature at 2 meters above ground and wind speed during the Pre-Lockdown, Lockdown, and Post-Lockdown periods in 2020 and the same periods in 2019.

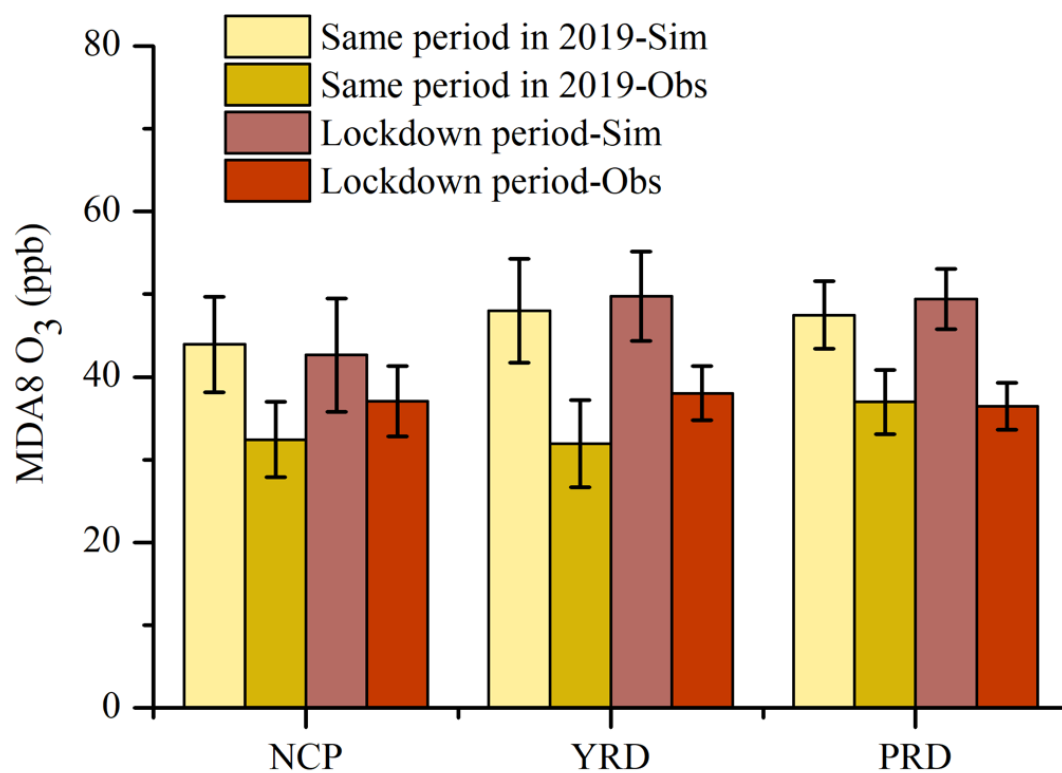


Figure S3: Simulated and observed mean MDA8 O₃ in the three key regions during the Lockdown and the same period in 2019.

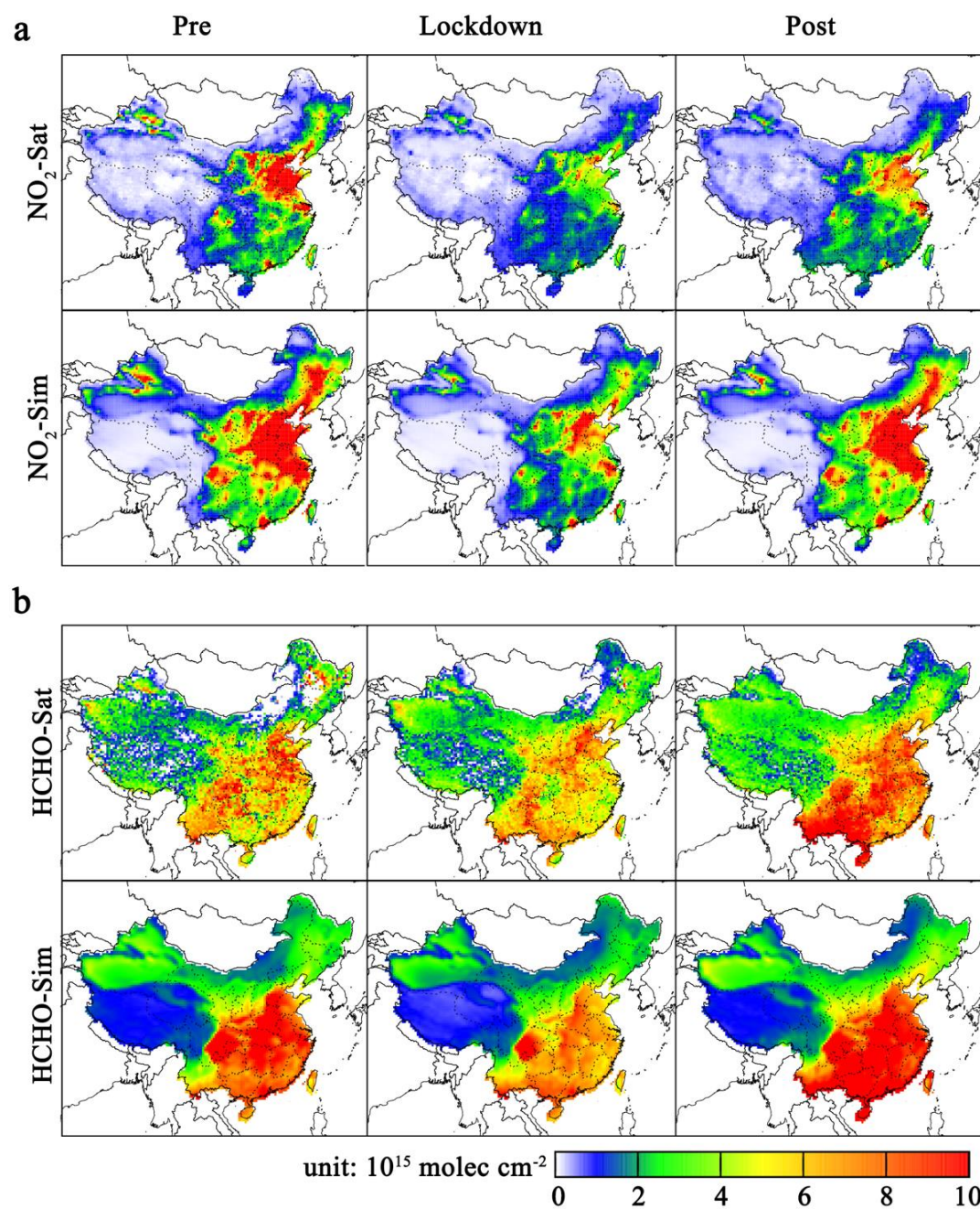


Figure S4: Simulated and satellite observed spatial distribution of NO₂ and HCHO during the Pre-Lockdown, Lockdown, and Post-Lockdown periods in 2020.

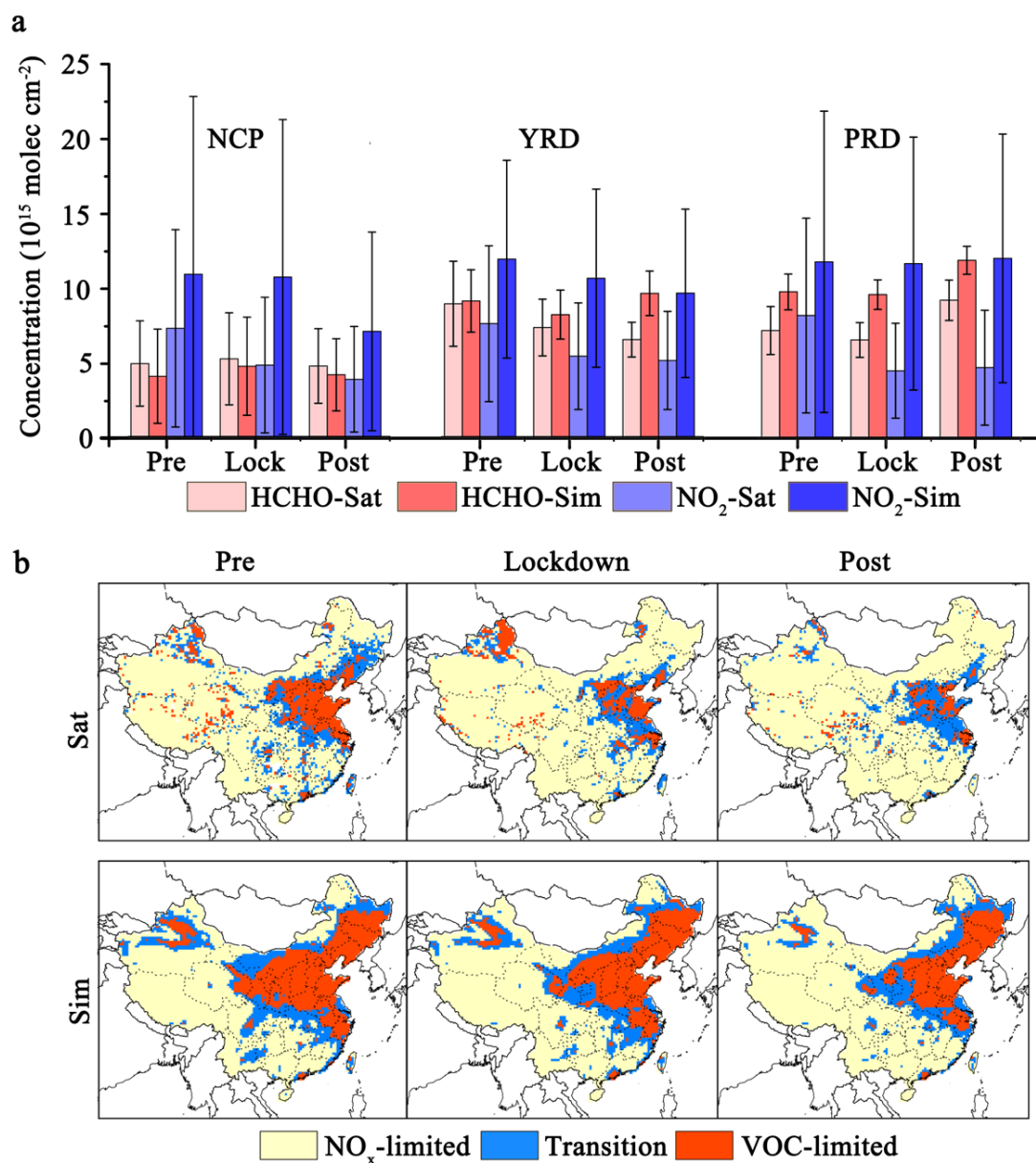


Figure S5: The spatial distribution of NO₂ and HCHO and the O₃ formation regime in China (a) The simulated and Tropomi satellite observed results of NO₂ and HCHO column concentrations in NCP, YRD, and PRD regions during the same periods of Pre-Lockdown, Lockdown, and Post-Lockdown in 2019. (b) The simulated and satellite observed results of O₃ formation regime in the troposphere during the same periods of Pre-Lockdown, Lockdown, and Post-Lockdown in China.

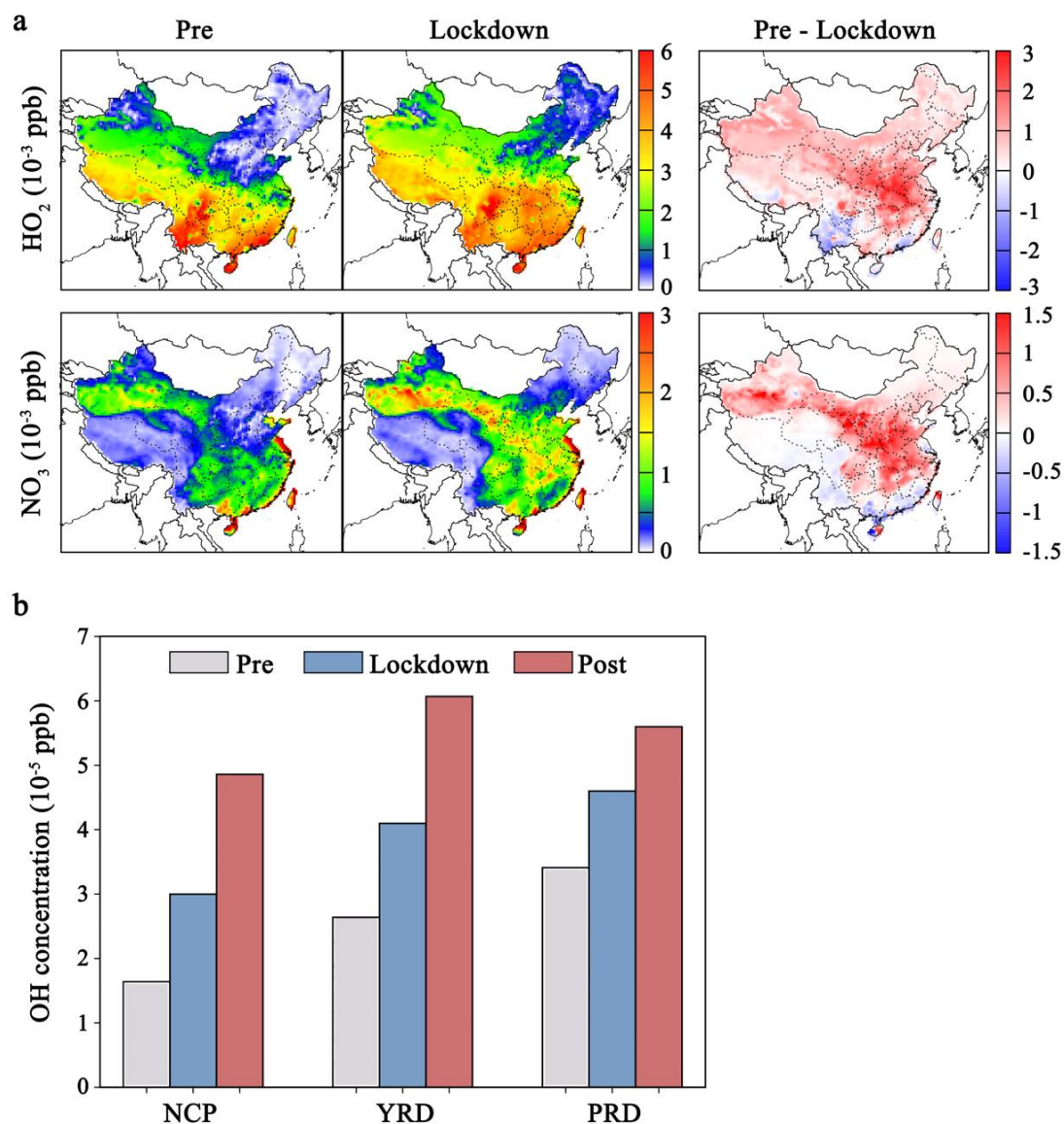


Figure S6: Major oxidants changes during the Pre-lockdown and Lockdown. (a) Regional variation of the HO_2 and NO_3 radicals during the Pre-Lockdown and Lockdown periods in 2020. (b) The variation in the OH radical concentrations during the Pre-Lockdown, Lockdown, and Post-Lockdown periods in the NCP, YRD, and PRD regions in 2020.

Table S1: Emission reduction ratios of different air pollutants at the provincial level during the Lockdown ¹⁰.

Province	CO	NO _x	SO ₂	VOC	PM _{2.5}	BC	OC
Beijing	22%	45%	26%	45%	18%	46%	8%
Tianjin	21%	38%	20%	41%	14%	22%	6%
Hebei	15%	45%	16%	36%	12%	17%	5%
Shanxi	18%	40%	20%	33%	16%	19%	10%
Inner Mongolia	14%	29%	15%	34%	13%	16%	6%
Liaoning	21%	40%	28%	36%	16%	28%	8%
Jilin	16%	39%	23%	34%	13%	18%	5%
Heilongjiang	17%	37%	27%	28%	13%	15%	7%
Shanghai	35%	48%	42%	45%	34%	54%	42%
Jiangsu	23%	50%	26%	41%	16%	35%	7%
Zhejiang	41%	50%	29%	45%	30%	49%	20%
Anhui	14%	56%	22%	31%	11%	22%	4%
Fujian	29%	51%	30%	42%	19%	31%	7%
Jiangxi	24%	53%	21%	43%	19%	30%	9%
Shandong	23%	50%	25%	39%	19%	35%	9%
Henan	23%	57%	22%	41%	18%	35%	8%
Hubei	19%	55%	23%	35%	16%	23%	10%
Hunan	22%	51%	25%	36%	20%	24%	15%
Guangdong	38%	50%	33%	46%	27%	42%	13%
Guangxi	24%	50%	28%	39%	17%	27%	5%
Hainan	24%	44%	25%	36%	14%	25%	4%
Chongqing	18%	53%	32%	37%	14%	20%	4%
Sichuan	16%	50%	27%	33%	9%	15%	3%
Guizhou	24%	39%	25%	30%	22%	25%	20%
Yunnan	24%	51%	25%	41%	18%	21%	8%
Tibet	16%	35%	15%	35%	14%	14%	5%
Shaanxi	19%	45%	18%	34%	13%	22%	5%
Gansu	13%	47%	16%	29%	9%	13%	3%
Qinghai	23%	46%	22%	39%	20%	20%	7%
Ningxia	24%	36%	24%	39%	20%	23%	8%
Xinjiang	16%	35%	15%	35%	14%	14%	5%

Table S2: Model performance of meteorological parameters temperature (T), wind speed (WS), wind direction (WD), and relative humidity (RH) from January to March in 2020 (PRE is mean prediction; OBS is mean observation; MB is mean bias; GE is gross error; and RMSE is root mean square error).

		Jan	Feb	Mar	Benchmark*
T (K)	PRE	276.55	278.15	282.79	
	OBS	277.54	279.47	284.22	
	MB	-0.93	-1.25	-1.35	$\leq \pm 0.5$
	GE	2.78	2.89	2.80	≤ 2.0
	RMSE	3.79	3.93	3.84	
WS (m/s)	PRE	4.55	4.66	4.68	
	OBS	3.24	3.38	3.51	
	MB	1.32	1.28	1.17	$\leq \pm 0.5$
	GE	1.89	1.90	1.83	≤ 2.0
	RMSE	2.45	2.45	2.35	≤ 2.0
WD (°)	PRE	191.94	197.16	197.74	
	OBS	188.06	186.69	189.12	
	MB	8.17	11.30	10.06	$\leq \pm 10$
	GE	45.67	45.08	44.55	≤ 30
	RMSE	62.71	62.18	61.87	≤ 30
RH (%)	PRE	72.27	69.27	67.48	
	OBS	74.24	70.96	70.08	
	MB	-1.97	-1.69	-2.60	
	GE	11.12	11.63	12.30	
	RMSE	14.41	15.19	15.98	

Note: * are benchmarks limits suggested by Emery et al. (2001), data which do not fall under the limits are shown as bold.

Table S3: Model performance on pollutants concentration in China from January to March 2020. (MNB: mean normalized bias; MNE: mean normalized error; MFB: mean fractional bias; and MFE: mean fractional error).

		Jan	Feb	Mar	Criteria
O ₃ -1h (ppb)	OBS	64.68	64.95	67.10	
	PRE	69.54	67.28	75.52	
	MNB	0.08	0.04	0.13	$\leq \pm 0.15$
	MNE	0.12	0.09	0.17	≤ 0.3
	MFB	0.07	0.03	0.11	
	MFE	0.11	0.09	0.15	
O ₃ -8h (ppb)	OBS	42.56	43.76	46.61	
	PRE	49.89	50.92	55.75	
	MNB	0.19	0.18	0.21	$\leq \pm 0.15$
	MNE	0.24	0.21	0.24	≤ 0.3
	MFB	0.15	0.15	0.17	
	MFE	0.20	0.19	0.21	
NO ₂ (ppb)	OBS	14.98	9.13	12.26	
	PRE	10.43	6.66	10.50	
	MNB	-0.15	-0.08	0.03	
	MNE	0.64	0.73	0.73	
	MFB	-0.48	-0.48	-0.36	
	MFE	0.73	0.80	0.73	
SO ₂ (ppb)	OBS	4.53	3.61	3.46	
	PRE	8.83	5.88	6.47	
	MNB	2.03	1.47	1.66	
	MNE	2.38	1.91	2.05	
	MFB	0.32	0.15	0.22	
	MFE	0.86	0.85	0.84	

Table S4: Model performance of meteorological parameters temperature (T), wind speed (WS), wind direction (WD), and relative humidity (RH) from January to March in 2019 (PRE is mean prediction; OBS is mean observation; MB is mean bias; GE is gross error; and RMSE is root mean square error).

		Jan	Feb	Mar	Benchmark*
T (K)	PRE	276.48	278.04	283.04	
	OBS	276.99	278.74	283.91	
	MB	-0.43	-0.61	-0.78	$\leq \pm 0.5$
	GE	2.64	2.65	2.55	≤ 2.0
	RMSE	3.64	3.61	3.52	
WS (m/s)	PRE	4.77	4.52	4.64	
	OBS	3.46	3.39	3.56	
	MB	1.32	1.13	1.08	$\leq \pm 0.5$
	GE	1.93	1.80	1.77	≤ 2.0
	RMSE	2.50	2.35	2.30	≤ 2.0
WD (°)	PRE	208.85	196.46	205.49	
	OBS	198.21	189.31	194.23	
	MB	12.52	9.68	11.61	$\leq \pm 10$
	GE	44.53	45.57	44.30	≤ 30
	RMSE	61.42	62.56	61.33	≤ 30
RH (%)	PRE	67.75	68.41	64.31	
	OBS	72.39	72.88	68.12	
	MB	-4.64	-4.47	-3.81	
	GE	11.92	11.88	12.24	
	RMSE	15.92	15.46	15.80	

Note: * are benchmarks limits suggested by Emery et al. (2001), data which do not fall under the limits are shown as bold.

Table S5: Model performance on pollutants concentration in China from January to March 2019.
(MNB: mean normalized bias; MNE: mean normalized error; MFB: mean fractional bias; and MFE: mean fractional error).

		Jan	Feb	Mar	Criteria
O ₃ -1h (ppb)	OBS	66.51	67.69	67.03	
	PRE	72.86	74.08	79.14	
	MNB	0.11	0.11	0.19	$\leq \pm 0.15$
	MNE	0.15	0.16	0.21	≤ 0.3
	MFB	0.09	0.09	0.16	
	MFE	0.14	0.15	0.18	
O ₃ -8h (ppb)	OBS	42.66	42.95	48.14	
	PRE	52.57	52.03	60.37	
	MNB	0.25	0.23	0.27	$\leq \pm 0.15$
	MNE	0.27	0.28	0.30	≤ 0.3
	MFB	0.20	0.18	0.21	
	MFE	0.23	0.23	0.24	
NO ₂ (ppb)	OBS	19.77	13.00	15.84	
	PRE	12.88	11.55	11.24	
	MNB	-0.23	0.18	-0.15	
	MNE	0.61	0.83	0.69	
	MFB	-0.55	-0.27	-0.52	
	MFE	0.75	0.72	0.79	
SO ₂ (ppb)	OBS	5.98	4.54	4.16	
	PRE	10.56	7.27	7.30	
	MNB	1.92	1.55	1.58	
	MNE	2.25	1.96	1.99	
	MFB	0.32	0.19	0.18	
	MFE	0.84	0.83	0.83	

Table S6: Source apportionment analysis of NO₂ and HCHO during the Pre-Lockdown, Lockdown, and Post-Lockdown periods in 2020. Units are 10¹⁵ molec/cm².

Pre-Lockdown	Backg round	Power	Agricul ture	Industr y	Reside ntial	Transp ortation	Others	Total
NO ₂ (NCP)	0.08	2.77	0.0	3.97	0.74	2.68	0.08	10.32
NO ₂ (YRD)	0.08	2.80	0.0	4.18	0.57	4.10	0.23	11.96
NO ₂ (PRD)	0.11	1.90	0.0	2.78	0.14	4.09	2.09	11.11
HCHO(NC P)	2.57	0.0	0.0	0.52	0.75	0.28	0.12	4.24
HCHO(YR D)	5.24	0.0	0.0	1.09	1.46	0.59	0.48	8.86
HCHO(PR D)	6.96	0.0	0.0	0.82	0.43	0.53	0.89	9.63
Lockdown	Backg round	Power	Agricul ture	Industr y	Reside ntial	Transp ortation	Others	Total
NO ₂ (NCP)	0.09	1.15	0.0	1.82	0.32	1.27	0.06	4.71
NO ₂ (YRD)	0.07	0.95	0.0	1.56	0.21	1.71	0.24	4.74
NO ₂ (PRD)	0.10	0.76	0.0	1.18	0.07	2.02	2.13	6.26
HCHO(NC P)	2.44	0.0	0.0	0.31	0.42	0.17	0.08	3.41
HCHO(YR D)	4.70	0.0	0.0	0.51	0.64	0.31	0.46	6.62
HCHO(PR D)	6.50	0.0	0.0	0.33	0.17	0.26	0.99	8.25
Post-Lockdown	Backg round	Power	Agricul ture	Industr y	Reside ntial	Transp ortation	Others	Total
NO ₂ (NCP)	0.08	1.83	0.0	3.01	0.33	2.03	0.07	7.35
NO ₂ (YRD)	0.07	2.39	0.0	3.83	0.26	3.56	0.28	10.39
NO ₂ (PRD)	0.09	1.85	0.0	2.73	0.10	3.63	2.63	11.03
HCHO(NC P)	3.40	0.0	0.0	0.36	0.27	0.18	0.10	4.31
HCHO(YR D)	7.21	0.0	0.0	0.76	0.46	0.40	0.65	9.48
HCHO(PR D)	9.24	0.0	0.0	0.49	0.12	0.32	1.31	11.48

Table S7: The percentage of each O₃ formation regime type in the NCP, YRD and PRD regions during the Pre-Lockdown, Lockdown, and Post-Lockdown periods in 2020.

Pre-Lockdown	Tro			Sim		
	NO _x -limited	Transition	VOC-limited	NO _x -limited	Transition	VOC-limited
NCP	0.11	0.22	0.67	0.13	0.15	0.72
YRD	0.37	0.45	0.17	0.03	0.31	0.66
PRD	0.31	0.41	0.28	0.31	0.23	0.46

Lockdown	Tro			Sim		
	NO _x -limited	Transition	VOC-limited	NO _x -limited	Transition	VOC-limited
NCP	0.56	0.36	0.08	0.20	0.28	0.52
YRD	0.65	0.33	0.02	0.29	0.55	0.16
PRD	0.69	0.31	0.0	0.44	0.28	0.28

Post-Lockdown	Tro			Sim		
	NO _x -limited	Transition	VOC-limited	NO _x -limited	Transition	VOC-limited
NCP	0.48	0.36	0.16	0.09	0.26	0.65
YRD	0.57	0.38	0.05	0.09	0.39	0.51
PRD	0.74	0.0	0.26	0.28	0.36	0.36